


# Ultrahigh coercivity and core–shell microstructure achieved in oriented Nd–Fe–B thin films diffusion-processed with Dy-based alloys

Tongbo Zhang<sup>1,2</sup> · Xiaoqian Zhou<sup>1,2</sup> · Dedong Yu<sup>1,2</sup> · Yanqing Fu<sup>1,2</sup> · Guojian Li<sup>1</sup> · Weibin Cui<sup>1,2</sup>  · Qiang Wang<sup>1</sup>

Received: 30 September 2016 / Accepted: 15 December 2016 / Published online: 6 January 2017  
© Springer-Verlag Berlin Heidelberg 2017

**Abstract** Ultrahigh ambient coercivities of  $\sim 4$  T were achieved in Nd–Fe–B benchmark thin film with coercivity of 1.06 T by diffusion-processing with Dy, Dy<sub>70</sub>Cu<sub>30</sub> and Dy<sub>80</sub>Ag<sub>20</sub> alloy layer. High texture and good squareness were obtained. In triple-junction regions, Dy element was found to be immiscible with Nd element. Microstructure observation indicated the typical gradient elementary distribution. Unambiguous core/shell microstructure was characterized by transition electron microscopy. Due to the enhanced ambient coercivity, the coercivity temperature stability was also substantially increased.

## 1 Introduction

Nd–Fe–B-based sintered magnets, which were discovered in 1980s, had shown the comprehensive advantages than other permanent magnets. Usually, the coercivities of commercial sintered magnets were between 1 and 1.5 T. Recently, there was a strong need of high-performance Nd–Fe–B sintered magnets used in traction motors in (hybrid) electric vehicles (HEV) and wind power generators. To meet such application, the coercivity should be around 3 T at room temperature, possibly leading to the coercivity of over 0.8 T at working temperature, for example, at

120–180 °C. These requirements were much higher than the performances of current commercialized Nd–Fe–B sintered magnets. A general approach for improve the performance of sintered magnets was to refine the grain size of the Nd<sub>2</sub>Fe<sub>14</sub>B phase [1, 2]. However, Nothnagel reported that there was a critical grain size of around 3  $\mu\text{m}$ , at which the  $H_{cj}$  drastically decreased with further refinement [2] due to appearance of a large fraction of neodymium oxides including dhcp-Nd, fcc-NdO and hcp-Nd<sub>2</sub>O<sub>3</sub> [3]. Recently, by a combination of hydrogenation–disproportionation–desorption–recombination (HDDR) process, desorption–recombination (DR) process and jet milling process, the critical size of Nd<sub>2</sub>Fe<sub>14</sub>B grains was further reduced down to submicrometer scale. And the coercivity of 1.32 T and remanence of 0.73 T had been achieved [4]. But there were still many difficulties for further improvement on the coercivity by only using grain refinement.

Another industrial solution was to add Dy or Tb, such heavy rare-earth elements into Nd–Fe–B magnets during melting process. Therefore, by increasing the ambient coercivity to about 3 T, the coercivity at the operation temperature of 200 °C was possibly around 1 T. Since partial Dy or Tb replacement increased the magnetocrystalline anisotropy ( $\mu_0 H_A$ ) of 2:14:1 phase, the coercivity and its thermal stability were therefore improved. However, due to the antiparallel alignment of Dy or Tb moments with Fe moments, the magnetization was substantially decreased. Later, the GBs were found to play more critical role on influencing the coercivities since the  $\mu_0 H_A$  of the grain surface region was usually damaged by defects. Grain boundary diffusion process (GBDP) technique was developed to increase the coercivity more efficiently and economically. Various heavy-rare-earth-based alloys or inorganic salts, such as Dy [5], Dy–Cu [6], Dy–Co [7], Dy–Fe–Cu [8], DyF<sub>3</sub> [9, 10], TbF<sub>3</sub> [11] and TbCl<sub>3</sub>

✉ Weibin Cui  
cuiweibin@epm.neu.edu.cn

<sup>1</sup> Key Laboratory of Electromagnetic Processing of Materials (EPM), Ministry of Education, Northeastern University, Shenyang 110819, China

<sup>2</sup> Department of Physics and Chemistry of Materials, School of Materials Science and Engineering, Northeastern University, Shenyang 110819, China

[12], were ever tried. Generally, a maximum increment of coercivity about  $\sim 1$  T could be achieved in bulk magnet after diffusion process with Dy-based alloys [5–10].  $\text{Nd}_2\text{Fe}_{14}\text{B}$ -core/(Nd, HRE) $_2\text{Fe}_{14}\text{B}$ -shell (HRE = Tb, Dy) structure, which was assumed to be the reason for coercivity enhancement, was not well confirmed by the microstructural observation. On the other hand, it is technically meaningful to investigate how much the potential coercivity enhancement would be obtained by diffusion-processing with Dy-based alloys. Therefore, we carried out the diffusion process in Nd–Fe–B thin films with Dy-based alloys. The potential coercivity enhancement was studied. The resultant microstructure evolution was characterized by TEM observation with different elementary preferred distribution. The coercivity temperature coefficient was enhanced due to the increased coercivity.

## 2 Experiments

A Ta(20 nm)/ $\text{Nd}_{14}\text{Fe}_{77}\text{B}_9$ (100 nm)/Ta(20 nm) benchmark thin film was firstly prepared. The depositions of Ta underlayer and coverlayer were carried out at room temperature.  $\text{Nd}_{14}\text{Fe}_{77}\text{B}_9$ (100 nm) layer was deposited at 873 K in a base vacuum better than  $5 \times 10^{-5}$  Pa. To carry out diffusion process, Ta(20 nm)/ $\text{Nd}_{14}\text{Fe}_{77}\text{B}_9$ (100 nm)/diffusion layer(10 nm)/Ta(20 nm) (diffusion layer = Dy,  $\text{Dy}_{70}\text{Cu}_{30}$  or  $\text{Dy}_{80}\text{Ag}_{20}$  alloy layer) were prepared and post-annealed at 923 K for 30 min. The constituent phases were characterized by X-ray diffraction (XRD) using Cu  $K_\alpha$  radiation. The cross-sectional morphologies were achieved by Gatan  $G^2$  F30 with energy filter. The hysteresis loops along the out-of-plane (OOP) and in-plane (IP) directions were measured by the superconducting quantum interference devices (SQUID) with temperature up to 400 K.

## 3 Results and discussion

Figure 1 shows the X-ray diffraction (XRD) patterns of benchmark film with those of diffusion-processed films. In the benchmark film, the diffraction peaks at  $2\theta \approx 29^\circ$ ,  $2\theta \approx 44^\circ$  and  $2\theta \approx 62^\circ$  with strong intensities indicate the (004) plane, (006) plane and (008) plane of 2:14:1 phase, showing the strong textured microstructure. After diffusion-processing with Dy(10 nm),  $\text{Dy}_{70}\text{Cu}_{30}$ (10 nm) or  $\text{Dy}_{80}\text{Ag}_{20}$ (10 nm) alloy layers, the intensity of (105) peak at  $2\theta \approx 38^\circ$  is increased. Besides, an additional peak at  $2\theta \approx 31^\circ$  is observed, which is a characteristic peak of the Nd-rich phase with the double-hexagonal close-packed structure. However, some other peaks are also observed after diffusion process, indicating that the texture degree is slightly degraded.

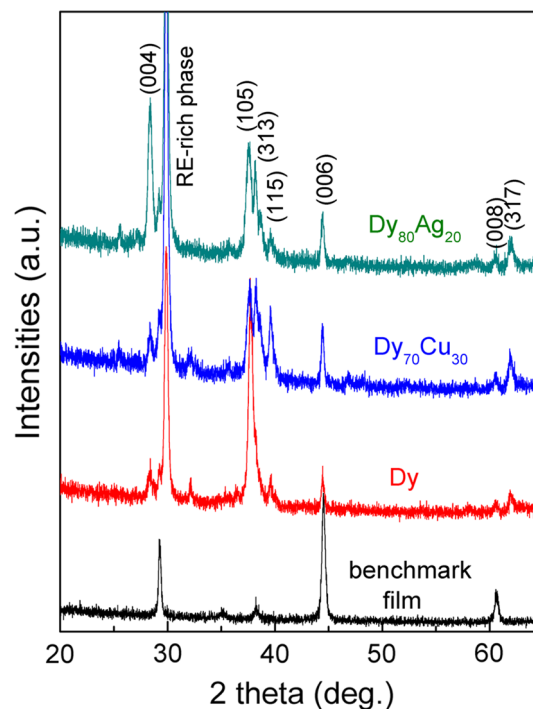
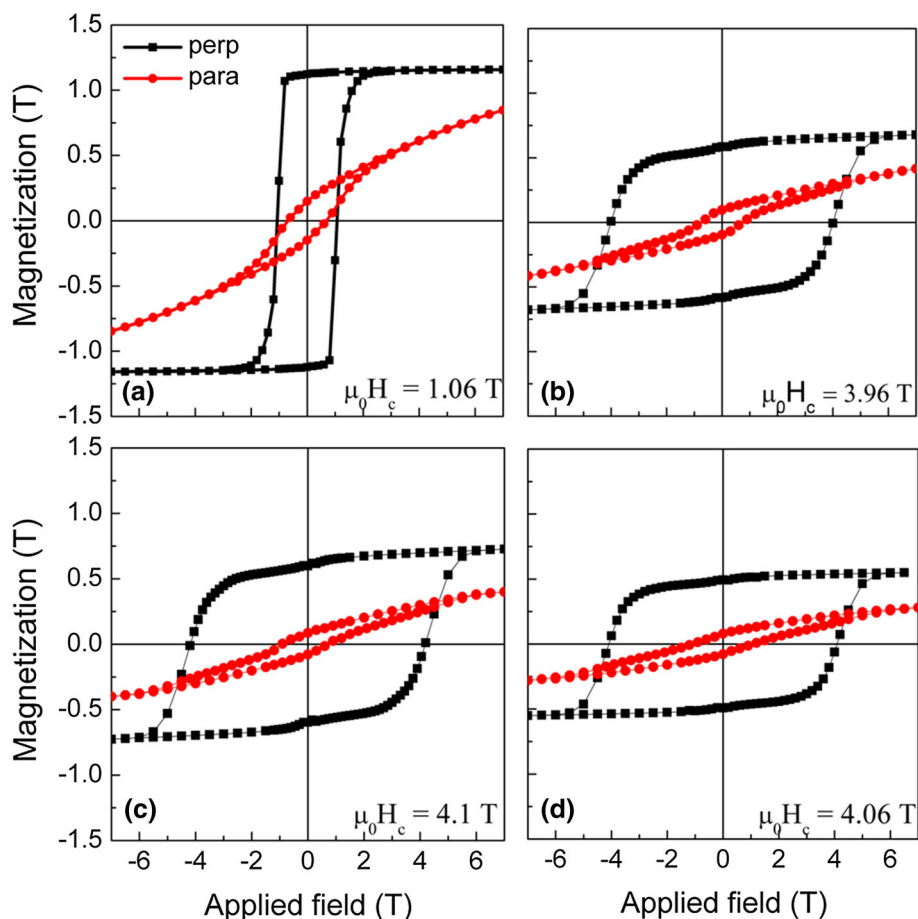


**Fig. 1** X-ray diffraction (XRD) patterns of Ta(20 nm)/ $\text{Nd}_{14}\text{Fe}_{77}\text{B}_9$ (100 nm)/Ta(20 nm) benchmark film compared with those of the films diffusion-processed with Dy(10 nm),  $\text{Dy}_{70}\text{Cu}_{30}$ (10 nm) and  $\text{Dy}_{80}\text{Ag}_{20}$ (10 nm) alloy layers

Figure 2 compares the hysteresis loops of benchmark film compared with those of diffusion-processed films. Due to the well-textured microstructure as indicated from XRD patterns, different magnetization behaviors along out-of-plane (OOP) direction and in-plane (IP) direction of the substrate are observed. Good squareness is achieved along OOP direction. However, coercivity in the benchmark film is only 1.06 T due to the lack of Nd-rich phase as seen from XRD pattern. After diffusion process with Dy(10 nm) layers, the anisotropic magnetization behavior is not changed. High squareness is maintained. The coercivity is almost quadrupled to 3.96 T. The magnetization behavior along IP direction is almost linear with reduced hysteresis, indicating the ultrahigh  $\mu_0 H_A$ . By diffusion-processing with  $\text{Dy}_{70}\text{Cu}_{30}$ (10 nm) and  $\text{Dy}_{80}\text{Ag}_{20}$ (10 nm) alloy layers, a maximum coercivity of 4.1 T has been achieved in Ta(20 nm)/ $\text{Nd}_{14}\text{Fe}_{77}\text{B}_9$ (100 nm)/ $\text{Dy}_{70}\text{Cu}_{30}$ (10 nm)/Ta(20 nm) film compared with 4.06 T in Ta(20 nm)/ $\text{Nd}_{14}\text{Fe}_{77}\text{B}_9$ (100 nm)/ $\text{Dy}_{70}\text{Ag}_{30}$ (10 nm)/Ta(20 nm) film. The analogue linear magnetization behaviors are observed along IP direction thanks to the diffusion process using Dy-based alloys. However, the saturation magnetizations of these films are substantially decreased. One reason is because that the magnetic moments of Dy are antiparallel with those of Nd and Fe moments. Nd replaced by Dy in 2:14:1 phase will go to

**Fig. 2** Hysteresis loops of Ta(20 nm)/Nd<sub>14</sub>Fe<sub>77</sub>B<sub>9</sub>(100 nm)/Ta(20 nm) benchmark film and those of diffusion-processed films with Dy(10 nm), Dy<sub>70</sub>Cu<sub>30</sub>(10 nm) and Dy<sub>80</sub>Ag<sub>20</sub>(10 nm) alloy layers



grain boundary regions and form nonmagnetic phases. The possibly existing nonmagnetic rare-earth oxides will also reduce the saturation magnetization, which is another reason for low magnetizations after diffusion process.

The changes in the magnetic properties are always related to the microstructure evolution. Figure 3a shows the cross-sectional morphology of benchmark film. The rough surface with particulate morphology was observed. From the Nd-loss image (Fig. 3b), the bright regions which indicate the Nd-rich phase are observed in the GB regions. Magnetic isolation between neighboring Nd<sub>2</sub>Fe<sub>14</sub>B grains is not sufficient by the inhomogeneous distribution of Nd-rich phase, leading to the poor coercivity. Figure 3c shows the high-magnification TEM image of the marked region in Fig. 3a. Clear lattice fringes are observed. The corresponding Fourier transform patterns are shown in Fig. 3d. The fast Fourier transform patterns are indexed as the (100) plane with an incident electronic beam along [100] axis. Therefore, the normal direction of the lattice fringes shown in Fig. 3c is [001] direction, which is the c axis of Nd<sub>2</sub>Fe<sub>14</sub>B grain as indicated in Fig. 3c. By diffusion-processing with Dy(10 nm) layer, cross-sectional morphology is not substantially changed as seen in Fig. 3e. From cross-

sectional Nd-loss image, on the top of the layer, Nd-rich region is observed along with neighboring Nd-lean regions and grain boundary as marked in Fig. 3f. However, in the corresponding Dy-loss image (Fig. 3g), the Nd-rich regions marked in Fig. 3f become Dy-lean, while those Nd-lean regions in Fig. 3f become Dy-rich as seen in Fig. 3g. From the dispersion of Nd-rich and Dy-rich regions, Dy is found to be not alloyed with Nd in the GB regions. Meanwhile, the thin Dy-rich shell is observed outside Nd<sub>2</sub>Fe<sub>14</sub>B grains, forming the Nd<sub>2</sub>Fe<sub>14</sub>B-core/(Nd, Dy)<sub>2</sub>Fe<sub>14</sub>B-shell structure. From the film top surface to the bottom, gradient Dy distribution is roughly formed, showing the typical composition distribution of diffusion-processed alloys.

Figure 4a, b shows the IP bright-field image and Nd-loss image of benchmark film, respectively. The GBs are clearly observed with grain size generally larger than 100 nm. Many regions consisting of Nd-rich phase are frequently observed in triple-junction regions. In the adjacent intergrain intersurfaces, they are also Nd-enriched. Such aggregation by Nd-rich phase in triple-junction regions is not the optimized microstructure for enhanced coercivity since low coercivity is obtained in benchmark film. Figure 4c shows the IP TEM image of

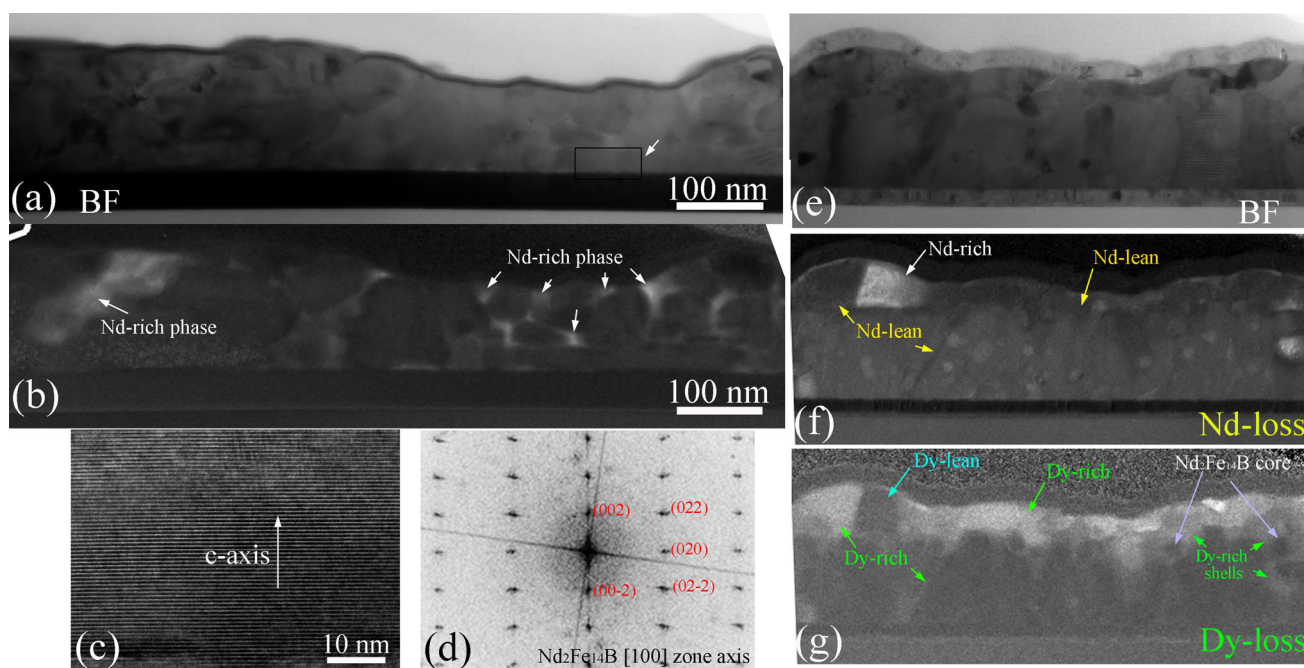


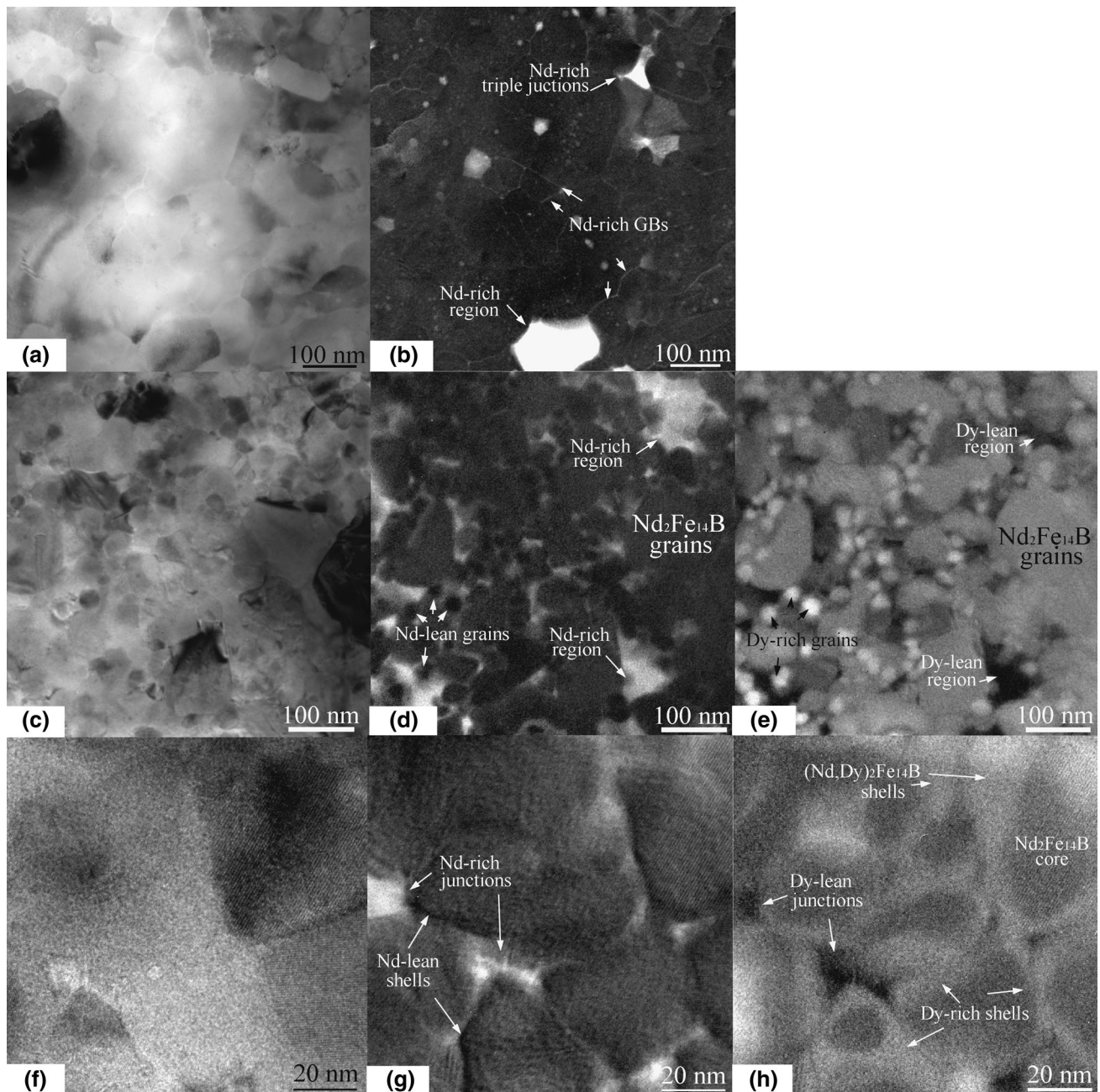
**Fig. 3** Cross-sectional bright-field image of **a** Ta(20 nm)/Nd<sub>14</sub>Fe<sub>77</sub>B<sub>9</sub>(100 nm)/Ta(20 nm) benchmark film and **b** corresponding Nd-loss image. **c** High-magnification image of the region marked in **a**, **d** corresponding Fourier transform patterns. **e** Cross-sectional bright-

field image of Ta(20 nm)/Nd<sub>14</sub>Fe<sub>77</sub>B<sub>9</sub>(100 nm)/Dy(10 nm)/Ta(20 nm) film and corresponding **f** Nd-loss image and **g** Dy-loss image

Ta(20 nm)/Nd<sub>14</sub>Fe<sub>77</sub>B<sub>9</sub>(100 nm)/Dy(10 nm)/Ta(20 nm) diffusion-processed thin film with the corresponding Nd-loss image and Dy-loss image. The granular morphology is seen with grain size smaller than 100 nm. After diffusion process, the Nd<sub>2</sub>Fe<sub>14</sub>B grains are isolated with Nd-rich phase. Large-size Nd-rich regions are also observed. Besides, some small-size grains as marked in Fig. 4d are observed to be Nd-lean. These Nd-lean grains and Nd-rich regions are identified to be Dy-rich and Dy-lean, respectively, as seen in Fig. 4e. From Fig. 4d and Fig. 4e, Nd composition in GB regions and triple-junction regions are higher than that in the interior region of 2:14:1 phase. As comparison, Dy composition is usually higher in 2:14:1 phase grain shell than that in GB regions or triple-junction regions. IP high-magnification TEM image of Ta(20 nm)/Nd<sub>14</sub>Fe<sub>77</sub>B<sub>9</sub>(100 nm)/Dy(10 nm)/Ta(20 nm) diffusion-processed thin film is shown in Fig. 4f together with the corresponding Nd-loss image (Fig. 4g) and Dy-loss image (Fig. 4h). Nd is displayed to be mainly enriched in the triple-junction region and GB regions in Fig. 4g, where Dy is usually lean as indicated in Fig. 4h. The elementary preferred distribution is different for Nd and Dy, showing the immiscible behavior as similar as reported in the diffusion-processed bulk magnets [5]. The gray contrast indicates the increased Dy composition in shell region of Nd<sub>2</sub>Fe<sub>14</sub>B grain than that in interior of Nd<sub>2</sub>Fe<sub>14</sub>B grain

and triple junctions, demonstrating the unambiguous formation of Nd<sub>2</sub>Fe<sub>14</sub>B-core/(Nd, Dy)<sub>2</sub>Fe<sub>14</sub>B-shell microstructure. Since Dy in the grain shell remedies the defects and provides high  $\mu_0 H_A$ , magnetically hardened shells behave the pinning sites for reversal domains and are responsible for the enhanced coercivity. For Cu and Ag elements, they are not considered to be diffused into Nd<sub>2</sub>Fe<sub>14</sub>B main phase and enriched in the grain boundaries, as observed in the case of diffusion-processing with Nd-based alloy [13–15].

Since the ambient coercivities are quadrupled to around 4 T at room temperature, the coercivity temperature dependences are compared in Fig. 5. In these films, the coercivities are decreased with increasing temperature due to reduced  $\mu_0 H_A$  with increasing temperature. The coercivity temperature coefficient is defined as  $\beta = [\mu_0 H_c(T_2) - \mu_0 H_c(T_1)] / [\mu_0 H_c(T_1) \times (T_2 - T_1)]$ . Here,  $\mu_0 H_c(T_2)$  and  $\mu_0 H_c(T_1)$  are the coercivities at temperature  $T_2$  and  $T_1$ , respectively. In the benchmark film, a low  $\beta$  of  $-0.5\%/K$  is obtained due to the low coercivity. After diffusion-processing with Dy-based alloy layers,  $\beta$  is greatly enhanced and ranged from  $-0.353$  to  $-0.371\%/K$ , thanks to the significantly increased ambient coercivity. Noting that  $\beta$  values of commercial sintered magnets are ranged from  $-0.45$  to  $-0.6\%/K$ , diffusion process with Dy-based alloy layer is obviously effective to enhance the coercivity and its thermal stability.



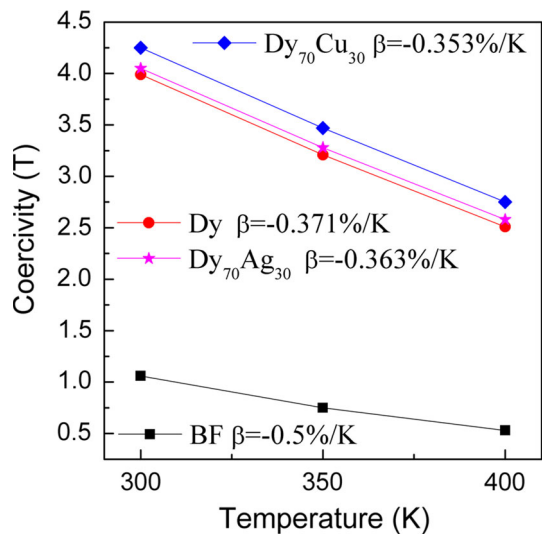
**Fig. 4** **a** In-plane bright-field image of Ta(20 nm)/Nd<sub>14</sub>Fe<sub>77</sub>B<sub>9</sub>(100 nm)/Ta(20 nm) benchmark film and **b** corresponding Nd-loss image; **c** In-plane bright-field image of Ta(20 nm)/Nd<sub>14</sub>Fe<sub>77</sub>B<sub>9</sub>(100 nm)/Dy(10 nm)/Ta(20 nm) film with **d** Nd-loss image and **e** Dy-loss

image. **f** High-magnification in-plane view image of Ta(20 nm)/Nd<sub>14</sub>Fe<sub>77</sub>B<sub>9</sub>(100 nm)/Dy(10 nm)/Ta(20 nm) film along with **g** Nd-loss image and **h** Dy-loss image

#### 4 Conclusions

Ambient coercivity of 1.06 T was achieved in the as-prepared Ta(20 nm)/Nd<sub>14</sub>Fe<sub>77</sub>B<sub>9</sub>(100 nm)/Ta(20 nm) benchmark film. After diffusion-processing with Dy(10 nm), Dy<sub>70</sub>Cu<sub>30</sub>(10 nm) or Dy<sub>80</sub>Ag<sub>20</sub>(10 nm) alloy layers, highly texture was maintained after diffusion

process and the ambient coercivities were quadrupled to around 4 T. The typical gradient composition distribution was observed from cross-sectional TEM images. The unambiguous Nd<sub>2</sub>Fe<sub>14</sub>B-core/(Nd, Dy)<sub>2</sub>Fe<sub>14</sub>B-shell microstructure was observed. The dealloying behavior between Dy and Nd in grain boundary regions was observed. Coercivity thermal stability was substantially



**Fig. 5** Coercivity temperature dependences of Ta(20 nm)/Nd<sub>14</sub>Fe<sub>77</sub>-B<sub>9</sub>(100 nm)/Ta(20 nm) benchmark film (BF) and the films diffusion-processed with Dy(10 nm), Dy<sub>70</sub>Cu<sub>30</sub>(10 nm) and Dy<sub>80</sub>Ag<sub>20</sub>(10 nm) alloy layers

increased due to the increased ambient coercivity by the diffusion process.

**Acknowledgements** This work was supported by National Natural Science Foundation of China under Grant No. 51501033, National Natural Science Funds for Distinguished Young Scholar under Grant

No. 51425401 and Fundamental Research Funds for the Central Universities under Grant No. 140901001.

## References

1. R. Ramesh, G. Thomas, B.M. Ma, *J. Appl. Phys.* **64**, 6416 (1988)
2. P. Nothnagel, K.H. Muller, D. Eckert, A. Handsterin, *J. Magn. Magn. Mater.* **101**, 379 (1991)
3. W.F. Li, T. Ohkubo, K. Hono, *Acta Mater.* **57**, 1337 (2009)
4. M. Nakamura, M. Matsuura, N. Tezuka, S. Sugimoto, Y. Une, H. Kubo, M. Sagawa, *Appl. Phys. Lett.* **103**, 022404 (2013)
5. N. Watanabe, M. Itakura, M. Nishida, *J. Alloy Compd.* **557**, 1 (2013)
6. W.B. Cui, Y.Q. Fu, T. Liu, G.J. Li, Q. Wang, *J. Alloy Compd.* **686**, 101 (2016)
7. X.F. Zhang, S. Guo, C.J. Yan, L.W. Cai, R.J. Chen, D. Lee, Aru Yan, *Appl. Phys.* **115**, 17A757 (2014)
8. L.P. Liang, T.Y. Ma, P. Zhang, J.Y. Jin, M. Yan, *J. Magn. Magn. Mater.* **355**, 131 (2014)
9. F. Xu, L.T. Zhang, X.P. Dong, Q.Z. Liu, M. Komuro, *Scr. Mater.* **64**, 1137 (2011)
10. X. Tang, R. Chen, W. Yin, M. Lin, D. Li, Aru Yan, *IEEE Trans. Magn.* **49**, 3237 (2013)
11. M. Soderznic, M. Korent, K.Z. Soderznic, M. Katter, K. Üstüner, S. Kobe, *Acta Mater.* **115**, 278 (2016)
12. S. Guo, X.F. Zhang, G.F. Ding, R.J. Chen, D. Lee, A. Yan, *J. Appl. Phys.* **115**, 17A754 (2014)
13. W.B. Cui, K. Takahashi, K. Hono, *Acta Mater.* **59**, 7768 (2011)
14. W.B. Cui, K. Takahashi, K. Hono, *Adv. Mater.* **24**, 6530 (2012)
15. W.B. Cui, H. Sepehri-Amin, Y.K. Takahashi, K. Hono, *Acta Mater.* **84**, 405 (2015)